Open Ceramics 8 (2021) 100182

Contents lists available at ScienceDirect

Open Ceramics

journal homepage: www.sciencedirect.com/journal/open-ceramics

High heating rate sintering and microstructural evolution assessment using the discrete element method

Mirele Horsth Paiva Teixeira [a,d,*], Vasyl Skorych [a], Rolf Janssen [b], Sergio Yesid Gómez González [c], Agenor De Noni Jr [c], João Batista Rodrigues Neto [d], Dachamir Hotza [c,d], Maksym Dosta [a]

[a] Institute of Solids Process Engineering and Particle Technology (SPE), Hamburg University of Technology (TUHH), Hamburg, Germany
[b] Institute of Advanced Ceramics, Hamburg University of Technology (TUHH), Hamburg, Germany
[c] Department of Chemical and Food Engineering, Federal University of Santa Catarina (UFSC), Florianópolis, SC, Brazil
[d] Graduate Program in Materials Science and Engineering (PGMAT), Federal University of Santa Catarina (UFSC), Florianópolis, SC, Brazil

ARTICLE INFO

Keywords:
Rapid sintering
Discrete element simulation
Temperature gradient
Densification
Micromechanical modeling
Microstructure evolution

ABSTRACT

An original discrete element model for coupling thermo-mechanics with sintering is presented to disclose the thermo-micromechanical behavior of particulate systems and their densification process under rapid firing. This paper focuses on the numerical model formulation and application on the fast firing of Al_2O_3, including its verification with literature. Particular emphasis is given to the evolution of thermal and densification gradients over sintering conditions and sample length, zeroing in on the shrinkage evolution and the characteristic densification phenomena. Relationships between defects, microstructure, and sintering parameters are also explored. Finally, the time-dependent change of material microstructure concerning coordination number evolution, cohesive neck size distribution, gradients of temperature, and sample length are analyzed. The numerical results present good agreement with experimental data from the literature.

1. Introduction

Sintering is a process where a substance in a dispersed state is transformed into a solid body with a higher density. It is a critical step in the microstructural development of parts produced by powder technology [1–3]. Fast heating rates have attracted scientific and technological interest to obtain highly dense ceramics with fine-grained microstructure in periods as short as some minutes [4,5]. The main technological advantages of fast firing lie in the economic and environmental benefits of lower energy consumption per payload, lower emissions, reduced scrap and re-fire, lower labor costs, shorter production times, and more reliable product consistency [6–8].

Experimental procedures on fast firing ceramic systems are vastly found in the literature [9–15]. These studies focus on hardness, relative density, water absorption, bending strength, and microstructural features, essentially grain growth and phase evolution. García and collaborators [16] experimentally assessed the thermal gradients generated through an Al_2O_3 body and the resultant densification front throughout a fast sintering protocol. However, the determination of the thermal gradients was limited to low temperatures (up to 1050 °C). Thus, despite the significant progress in the area, it has been challenging to fully understand the rearrangement, the densification, and the heat transfer phenomena on particulate systems under rapid sintering via experimentation only.

Numerical approaches have played a crucial role in elucidating thermomechanical phenomena, contributing to the control and optimization of the materials processing chain. Namely, the finite element method (FEM), the finite volume method (FVM) and the discrete element method (DEM) have been applied to model thermal phenomena in fluidized and packed beds [17–31] as well as for modeling of isothermal sintering [32–38]. Nevertheless, scarce numerical studies on fast-firing, based on FEM and FVM essentially, are found in the literature [4,36,39]. Besides, in most cases, unrealistic assumptions are made, such as considering the green ceramic a non-porous body and the absence of shrinkage during the densification. Furthermore, the FEM and FVM are well known element-based approaches for continuum media. Thus, the behavior of individual particles is neglected by design, and the discretization of small particles in the mesh may have its

* Corresponding author. Institute of Solids Process Engineering and Particle Technology (SPE), Hamburg University of Technology (TUHH), Hamburg, Germany.
E-mail addresses: mirele.teixeira@tuhh.de, mireleteixeira@hotmail.com (M.H.P. Teixeira).

https://doi.org/10.1016/j.oceram.2021.100182
Received 9 July 2021; Received in revised form 29 August 2021; Accepted 3 September 2021
Available online 8 September 2021

accuracy diminished by the loss of microstructural information [4,37,39].

The DEM approach overcomes the aforementioned issues by accounting for the granulated nature of the powder that composes the green body. Each powder particle can be considered a discrete unit that interacts with its neighbors according to the appropriate sintering laws. This method offers the advantage of considering grain rearrangement effects by design [40]. It also allows accessing micro/mesoscopic properties such as position, velocity, contact area, and coordination number of every particle [41]. Many DEM-based studies of sintering processes were performed using the model proposed by Parhami & McMeeking [42] for free and pressure-assisted isothermal sintering. This model has been extensively applied to model particles [35,40,43–45] and pores [33,34] rearrangement, anisotropic [46,47] and constrained [38,48] sintering, as well as the evolution of heterogeneities/defects during sintering. The Parhami & McMeeking model [42] was extended to describe grain coarsening [43,49], to consider variable coordination numbers [37], and to model the elastic component of sintering besides viscous flow [50–52]. Lately, it was applied to the modeling of composites sintering [32,51,53]. Note that none of the preceding approaches addressed sintering under non-isothermal conditions, i.e., fast sintering, in which the high heating rates generate gradients of temperature that contribute significantly to microstructure development, densification, and final product properties.

In this contribution, we present an original model for coupling thermo-mechanics with sintering model (TMS) to further understand the thermo-micromechanical behavior of particulate systems and their microstructure evolution during sintering, especially under the non-isothermal procedure. The TMS model was developed based on the DEM and applied on a ceramic body of Al_2O_3. The main equations and assumptions were consistently described. Microstructural and thermal features were compared with experimental data. Relationships between defects, microstructure, and sintering parameters were explored. The time-dependent change of material microstructure concerning coordination number, cohesive neck size, gradients of temperature and sample length are also analyzed.

The simulation framework MUSEN [54] was used to perform the simulations, an open-source software widely used in DEM investigations [32–34,41,55,56]. This system supports parallel computing on GPU based on the CUDA platform, which significantly reduces computation time, thus efficiently simulating millions of discrete objects [34,54].

2. Thermo-mechanics coupled with sintering (TMS) model

2.1. Problem set-up

A transient heating process was assumed to determine the temperature field inside the solid body. Fast firing simulations were carried out in the temperature range of 1250–1350 °C. An instantaneous heating rate was applied to resemble the direct introduction of the sample into a pre-heated furnace at sintering temperature. Further decreases in the heating rate were considered to evaluate its relationship with microstructural development. The furnace was modeled only by the boundary conditions applied to the body surface. Its temperature was assumed to remain constant over the process, and heat losses between the sample and the enclosed environment were neglected.

The proposed TMS model was applied to an Al_2O_3 system and validated with previously published experimental results.The numerical sample was designed to preserve particle size and scale the compact dimensions down due to computational limitations. The specific heat capacity $c_p(T)$ and thermal conductivity $\kappa(T)$ of alumina were considered to be temperature-dependent [57] according to Eqn (1) and (2):

$$c_p(T) = 1117 + 0.14\,T - 411\,e^{-0.006\,T} \quad (1)$$

$$\kappa(T) = 5.85 + \frac{15360\,e^{-0.002\,T}}{T + 516} \quad (2)$$

where T is the particle temperature (°C).

Applying the TMS model, thermal and relative density gradients were assessed and correlated with the microstructure evolution. Moreover, defects were purposefully introduced inside the Al_2O_3 compact addressing their influence on the final microstructure and relationship with sintering parameters. Lastly, micromechanical features were estimated based on the evolution of the coordination number and the cohesive neck size distribution.

2.2. Heat transfer phenomena

Heat transfer was approached as a thermomechanical problem. The particles were assumed to be opaque grey emitting spherical bodies with identical chemical compositions. Only thermal energy was transferred. The production/consumption of heat due to chemical reactions and thermal expansion were neglected. The determination of a temperature field for each particle is computationally unfeasible since granular assemblies contain many objects. Therefore, the isothermal premise was adopted in which each particle has one temperature degree of freedom only. The TMS model considered the following heat transfer mechanisms:

- Radiation – among particles at the sample surface and their surroundings, which corresponds to furnace environment;
- Convection – between the stagnant air inside the furnace and particles on the sample surface;
- Conduction – pair-wise heat transfers between contacting particles.

The particles were grouped in two zones based on their position to consider the different heat transfer mechanisms: the outer layer where all the heat transfer mechanisms are active and the inner zone, where only interparticle conductive heat transfer occurs. Radiative and convective heat transfer was approximated to happen in the exposed area A_p of outer particles solely. Fig. 1 depicts the half-section view of the numerical sample highlighting the outer layer and the inner zone, along with an illustration of the heat transfer mechanisms considered in the TMS model.

2.2.1. Radiation

The amount of thermal energy emitted by the environment and absorbed on outer particles surface was calculated by the Stefan-Boltzmann law assuming isothermal surfaces (Eqn (3)). For the sake of simplicity and to reduce computational complexity, the representative contact area A_p (m^2) was approximated as the projection of each outer particle surface area facing the enclosing environment [39] (Eqn (4)).

$$Q^{rad} = \varepsilon\, A_p\, \sigma\, S_a \left(T_{env}^4 - T_{outer}^4\right) \quad (3)$$

$$A_p = \pi\, R^2 \quad (4)$$

Here Q^{rad} is the heat transfer rate by radiation (W), ε is the surface emissivity (−), σ is the Stefan-Boltzmann constant ($W/m^2{\cdot}K^4$), S_a is the parameter of scaling for mass-surface-dependent heat transfer (−), T_{env} is the environment temperature (K), T_{outer} is the outer particle temperature (K), and R is the particle radius (m). The detailed description of S_a is provided in Section 2.4.2. Eqn (3) admits that the furnace cavity is considered a black body and the radiative heat rate is uniformly distributed over the outer particles.

2.2.2. Convection

The convective heat transfer rate Q^{conv} (W) was calculated according to Newton's law of cooling by [4,39,58,59] by Eqn (5):

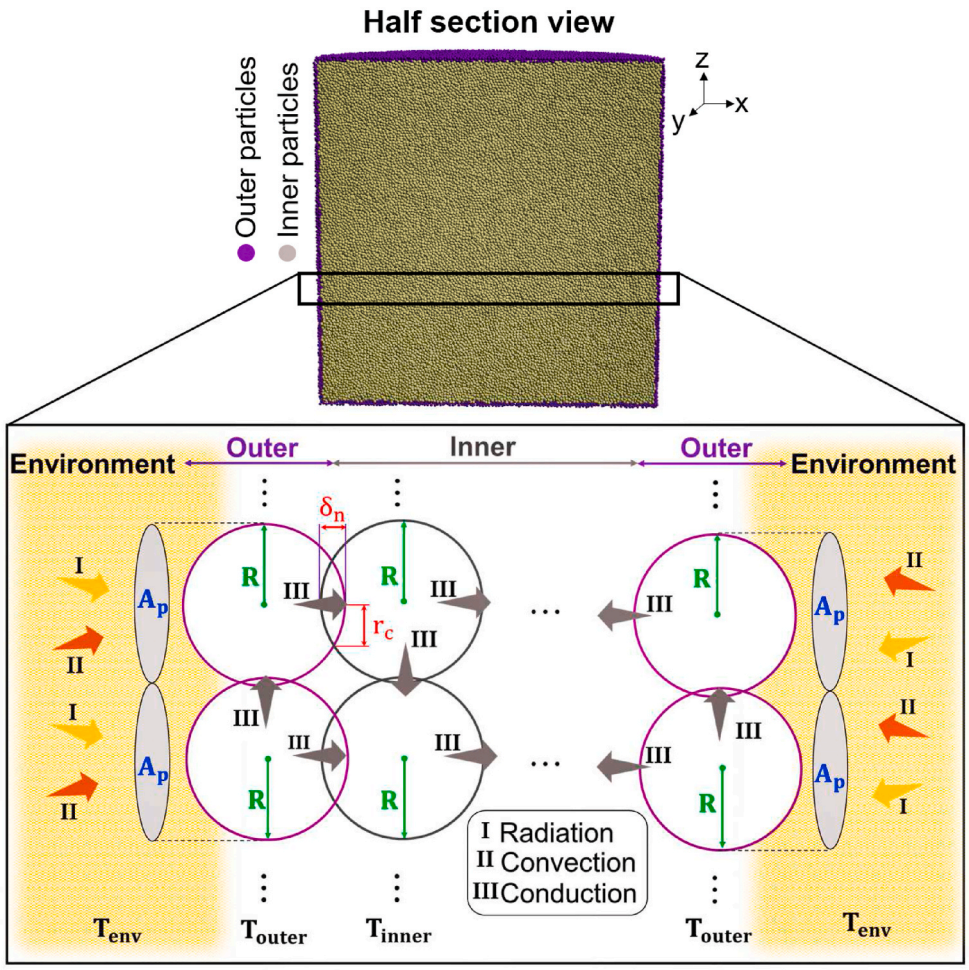

Fig. 1. Half section view of the 3D simulation sample highlights the outer layer and the inner zone, and illustrates the heat transfer mechanisms recognized in the TMS model. The arrows schematically depict the direction of heat flow. The heat flows from the hot environment surrounding (furnace atmosphere) to the outer particles through their representative contact area A_p. As the outer particles increase their temperature, heat is transferred particle by particle to the inner zone along the ceramic body through the interparticle contact with radius r_c.

$$Q^{conv} = A_p \;\; S_a \;\; h_c(T_{env} - T_{outer}) \tag{5}$$

here h_c is the convective heat transfer coefficient, typically in the range of 2–25 W/m^2.K for free convection in the air [59]. A_p and S_a are defined similarly as for radiation.

2.2.3. Conduction

The heat transfer rate by conduction Q^{cond} (W) in the contact between particles i and j was modeled by Eqn (6) [26,59–61]. The contact radius r_c (m) was derived from Coble geometric model (Eqn (7)) [33,62,63]. Note that i and j can be two outer particles, two inner particles, or an inner-outer contacting pair.

$$Q^{cond} = 2 \;\; r_c \cdot S_\ell \cdot f_{res}(\delta_n) \cdot \kappa(T) \cdot (T_j - T_i) \tag{6}$$

$$r_c = \sqrt{2\,R\,\delta_n} \tag{7}$$

Here S_ℓ is the scaling parameter for mass-length-dependent heat transfer (−), $\kappa(T)$ is the temperature-dependent thermal conductivity (W/m·K) of the particles, T_i and T_j are the particle temperatures (K), $f_{res}(\delta_n)$ is the thermal conduction resistivity factor, and δ_n is the normal overlap (m) estimated as the sum of particles radii diminished by the distance between the centers of contacting partners (s. Appendix). The calculation of S_ℓ is presented in Section 2.4.2. The existence of surface heterogeneities in the Al_2O_3 powder can restrict the effective contact area to a small fraction of the nominal contact area. The resistance to heat transfer at these contacts is often amplified [58,64,65] as a consequence. Thus, a resistivity factor f_{res} was included to consider this effect and was fitted to experimental data. Here the three different regimes were distinguished (s. Eqn (8)):

- Initial contact formation: at the early sintering stages, when the overlaps are smaller than the minimum threshold $\lambda_{min}R$, the conduction is limited by f^*_{res};
- Transition zone: as overlaps increase due to sintering, interparticle contacts become more effective. Hence, f_{res} effect gradually loses its importance. Accordingly, the thermal conductivity of contacting particles is linearly increased to the effective value in the range between $\lambda_{min}R$ and $\lambda_{max}R$;
- Late stages: when the upper limit of an overlap $\lambda_{max}R$ is reached.

$$f_{res}(\delta_n) = \begin{cases} f^*_{res}, \sigma_n \le \lambda_{min}R \\ f_{res} + \left(\dfrac{1 - f_{res}}{\lambda_{max} - \lambda_{min}}\right)\left(\dfrac{\delta_n}{R} - \lambda_{min}\right), \; \lambda_{min}R < \sigma_n < \lambda_{max}R \\ 1, \; \lambda_{max}R < \sigma_n \end{cases} \tag{8}$$

The conductive heat transfer model assumed quasi-static contacts and conduction by a stagnant interstitial medium was neglected under the assumption of having much smaller thermal conductivity than the particles.

2.2.4. Global heat transfer

The overall heat $\dot{Q}_{tot}$ transferred to a single particle is expressed by Eqn (9) as the sum of each thermal exchange experienced:

$$\dot{Q}_{tot} = \dot{Q}^{rad} + \dot{Q}^{conv} + \sum \dot{Q}^{cond} \tag{9}$$

Thus, the energy conservation equation for every particle at each

time-step was calculated by Eqn (10):

$$m_p c_p(T)\frac{dT}{dt} = \dot{Q}^{rad} + \dot{Q}^{conv} + \sum \dot{Q}^{cond} \quad (10)$$

here m_p (kg) is the particle mass.

Thereby, the incremental temperature change $T(t+\Delta t)$ (Eqn (11)) of a single particle at each time-step Δt was computed by increasing its previous temperature $T(t)$ by the overall heat transfer.

$$T(t+\Delta t) = T(t) + \Delta t\frac{\dot{Q}_{tot}}{m_p c_p(T)} \quad (11)$$

2.3. Interparticle interaction

Different contact models were used for the modeling of particle-particle interactions. Either the non-isothermal sintering model, the modified Hertz-Mindlin, or repulsive force contact models were applied depending on two parameters: the average temperature of contacted particles $\overline{T}$ and the normalized neck radius r_c/R.

As sintering is a thermally activated process, it is consistent (in a mono-sized single-phase system) to consider a minimum temperature at which its mechanisms begin to activate. García et al. [16] found out that up to 1050 °C, powder compacts of ultrafine alumina particles (~0.2 μm) showed no evidence of significant dimensional changes, that is, sintering mechanisms seemed to be still inactive up to this temperature. Hence, this temperature threshold has been implemented as a minimum temperature T_{min}^{sint}, below which no sintering occurs.

The relative density can be calculated using the evolution of r_c [63]. Thereby, a stop criterion for densification was defined based on the dimensionless parameter r_c/R, which was derived by normalizing the contact radius r_c over the particle radius R. Exploratory simulations confirmed that a fully dense sample was achieved at $r_c/R = 0.8$. Note that r_c/R is neither material nor number of particles dependent. The application of each contact model according to the specified conditions is expressed by Eqn (12):

$$\begin{cases} \overline{T} < T_{min}^{sint} & Hertz-Mindlin \\ \overline{T} \geq T_{min}^{sint} \text{ and } \frac{r_c}{R} \leq 0.8 & Sintering\ forces \\ \overline{T} \geq T_{min}^{sint} \text{ and } \frac{r_c}{R} > 0.8 & Repulsive\ force \end{cases} \quad (12)$$

2.3.1. Contact model

For low temperatures ($\overline{T} < T_{min}^{sint}$) at which sintering mechanisms are inactive, the modified non-linear Hertz-Mindlin contact force model was applied to allow particles to have rotational and translational degrees of freedom [25,66,67]. The formulated rheological model [25,67] treated particle interaction as a viscoelastic contact consisting of elastic stiffness K and viscous damping β components in normal F_n^{HM} (Eqn (13)) and tangential F_t^{HM} (Eqn (14)) directions. Note that both K and β parameters depend on the normal overlap (s. Appendix – Eqn A.2-4,5).

$$F_n^{HM} = K_n\delta_n^{HM} - \beta_n v_{rel,n} \quad (13)$$

$$F_t^{HM} = K_t\delta_t - \beta_t v_{rel,t} \quad (14)$$

Here δ_n^{HM} and δ_t are the interparticle overlaps (m) in normal and tangential directions. Compared to the standard formulation of the Hertz-Mindlin model, where the normal overlap is calculated based on the particle positions and their radii only, the present model incorporated an additional parameter δ_{pl} to describe flattening of initial contact surface and further "plastic"deformation caused by material sintering. The resulting normal overlap was calculated as Eqn (15):

$$\delta_n^{HM} = \delta_n - \delta_{pl} \quad (15)$$

After the densification stage, particles in the initial packing, which represent the green body, may have significant overlaps, and the direct application of the Hertz-Mindlin model may cause unphysical initial stresses. To avoid them, Eqn (16) was applied to consider all initial overlaps as initial flattening of the contact surface. The initial plastic deformation was calculated based on the particle positions at the initial time step.

$$\delta_{pl} = R_i + R_j - \left|\overrightarrow{X}_i(t_0) - \overrightarrow{X}_j(t_0)\right| \quad (16)$$

When the average temperature at the interparticle contact is larger than the sintering temperature ($\overline{T} \geq T_{min}^{sint}$) and the overlap is larger than the predetermined threshold (s. Eqn (12)), then only the repulsive force acts between the particles. This force was introduced to avoid sample over-densification, which could lead to non-physical negative porosities. The repulsive force acted in normal direction and was calculated as Eqn (17):

$$F_n^{rep} = K_n\delta_n^{rep} - \beta_n v_{rel,n} \quad (17)$$

$$\delta_n^{rep} = \delta_n - \delta_{max} \quad (18)$$

here δ_{max} is the maximal interparticle overlap in the fully densified state. This parameter has been identified as 80% of particle radius.

2.3.2. Non-isothermal solid-state sintering

When particles temperature is high enough ($\overline{T} \geq T_{min}^{sint}$), sintering starts. It is supposed that all the mechanical stresses previously caused due to compression or traction are relaxed and δ_{pl} is equaled to δ_n. Given account for non-isothermal conditions, the mass transfer parameter δ_b ($m^4 \cdot s/kg$) was discretized as a function of the average temperature $\overline{T}$ (K) of every pair-wise contacting particle at each time step by Eqn (19):

$$\delta_b = \frac{\Omega}{\kappa_B \overline{T}}\delta_b D_{0b}\, e^{\frac{-Q_b}{R_g \overline{T}}} \quad (19)$$

here Ω is the atomic volume (m^3), κ_B is the Boltzmann constant ($m^2 \cdot kg/K \cdot s^2$), δ_b is the grain boundary thickness (m), D_{0b} is the diffusion coefficient (m^2/s), Q_b is the activation energy (J/mol), and R_g is the universal gas constant (J/K·mol).

The average temperature $\overline{T}$ was computed by Eqn (20), where T_i and T_j are the temperatures of contacting particles.

$$\overline{T} = \frac{T_i + T_j}{2} \quad (20)$$

With the activation of sintering, forces in the normal F_n^{sint} (N) and tangential F_t^{sint} (N) directions appear [42,68]. Sintering normal force (Eqn (21)) consisted of an attractive component leading to densification, and a dissipative part, acting against the relative motion of the particles.

$$F_n^{sint} = F_{attractive} + F_{dissipative} = \frac{\alpha}{\beta}\pi R\,\gamma_s - \frac{\pi}{2\,\beta\delta_b}r_c^4\, v_{rel,n} \quad (21)$$

Here α and β are model parameters (−) related to the dominant mass transport mechanism, γ_s is the surface energy of particles (J/m^2), and $v_{rel,n}$ is the relative velocity (m/s) of the particles in the normal direction. Parameters α and β depend on the ratio of the grain boundary to the surface diffusion. According to Bouvard & McMeeking calculations [69], $\beta = 4$ may be used in all the cases. The parameter $\alpha = 9/2$ is applicable when grain-boundary diffusion is considered as a dominant sintering mechanism, whereas $\alpha = 5/2$ is suitable when surface diffusion prevails over grain-boundary diffusion. Grain-boundary diffusion was assumed to be the dominant mechanism of mass transfer during the sintering of Al_2O_3 [33,38,68,70]. Besides, it was previously demonstrated that the

dihedral angle has a limited effect on α and β [48,69]; therefore, it was neglected. The contact radius r_c was calculated as previously stated in Eqn (7).

The tangential sintering force F_t^{sint} consisted of a dissipative component opposing to the relative motion in the tangential direction $v_{rel,t}$ (m/s) as shown in Eqn (22):

$$F_t^{sint} = -\eta \frac{\pi R}{\beta \delta_b} r_c^2 v_{rel,t} \quad (22)$$

Here η is the viscous coefficient (−), typically set in the range between 0 and 0.1, which describes the resistance to slip (viscosity) of particle-particle contacts [46,48,68]. Furthermore, grain growth is essentially hindered during fast sintering due to rapid heating rates [5,71,72]; thus, it was neglected in the present model.

2.4. Generation of numerical samples

The numerical sample was produced by randomly placing spherical particles with a diameter of 0.2 μm into a cylindrical volume. The random generation was carried out via the force-biased algorithm implemented in the MUSEN software [54,73]. Particles were iteratively rearranged to minimize interparticle forces, which were calculated as a function of their normal overlaps. The rearrangement ended when the maximum overlap between all contacting bodies was smaller than a threshold specified by the user. It allows the generation of more homogeneous and isotropic packings. However, a minimal initial connectivity between particles is obtained, which does not represent the actual microstructure of the ceramic compacts. Therefore, after the placement of the particles was completed, the particle overlaps were increased to generate realistic initial connectivity by scaling particle size up by 1.5% of their primary diameter. This led to a final particle size of 0.203 μm, an increment of maximum overlap to 1.48% of the final particle size, and an average initial packing density of 0.62.

2.4.1. Specification of the outer layer

The determination of particles belonging to the outer layer was done in two stages based on the particle positions. Firstly, the number of particles belonging to the outer layer N_p^{outer} was calculated. To conserve overall heat transfer from the environment to the specimen, N_p^{outer} was approximated as the ratio between packing surface area A_{sample} (cylindrical shape) and the projected surface area A_p of a particle (s. Eqn (4)) by Eqn (23):

$$N_p^{outer} = \frac{A_{sample}}{A_p} \quad (23)$$

A total of 72,600 particles were estimated as belonging to the outer layer, considering the particles and sample dimensions presented in Table 1. In the second stage, the calculated number of particles was selected to define the outer layer. Two sets were composed of all the particles for the correct distribution of objects between the cylinder bases and side. The first included all particles sorted by their distance to the plane parallel to the base and intersecting the center of the cylinder (XY plane). The second had all particles sorted by their distance to the central axis (Z). Then, from each set, particles were selected in an amount corresponding to the ratio of the side area and area of the base of the cylinder, taking explicitly into account that the two obtained sets may intersect.

The TMS algorithm is presented in Fig. 2. In the first step, the initial interparticle overlap is taken as the plastic overlap representing the contact surface flattening. That allows avoiding any initial stresses in the material. Afterward, at each time step, the interparticle contacts are initially detected, and subsequently, followed by calculations of conductive heat transfer. For the particles in the outer layer, the additional convective and radiative transfer is computed. For each particle-particle contact, an average temperature is calculated and used as a criterion to determine what type of contact models will be used. The modified Hertz-Mindlin contact model is applied if the average temperature is below the minimum sintering temperature (s. Eqn (13)–(15)). When the average contact temperature reaches values equal to or higher than the minimum sintering temperature, and if the max densification criterion is below its threshold, the sintering model (s. Eqn (19)–(22)) is applied. Otherwise, if the temperature exceeds the minimum sintering temperature but the interparticle overlap is higher than the specific threshold, the repulsive force (s. Eqn (16)–(18)) is applied. The calculated forces and heat streams update particle properties such as positions, temperatures, and velocities. Finally, the simulation time is updated, and a new calculation iteration is started. The algorithm runs until the simulation end time is reached.

Table 1
Features of the numerical particles and the packing.

	Parameters	Symbol	Unit	Value
Alumina particles	Diameter	d_p	μm	0.203
	Density of alumina	ρ_{exp}	kg/m^3	$3.95{\cdot}10^3$
	Young modulus	E	Pa	$3.8{\cdot}10^{11}$
	Atomic volume	Ω	m^3	$8.47{\cdot}10^{-30}$
	Surface energy	γ_s	J/m^2	1.1
	Grain boundary thickness times diffusion parameter	$\delta_b D_{0b}$	m^3/s	$1.3{\cdot}10^{-8}$
	Activation energy	Q_b	J/mol	$4.75{\cdot}10^5$
Packing features	Initial packing size (height x diameter)	–	μm	22 × 22
	Average initial packing density	ρ_0	–	0.62
	Total number of particles	N^{tot}	–	1,157,970
	Number of particles in the outer layer	N_p^{outer}	–	72,600
	Maximum overlap	δ_{max}	μm	$3.01{\cdot}10^{-3}$
	Average overlap	$\bar{\delta}$	μm	$2.82{\cdot}10^{-3}$
	Total overlap	δ^{tot}	μm	9556.88

2.4.2. Scaling of mass and sample size

The size of the simulation time step directly influences the numerical stability of the solution [34,74]. As a means for speeding up DEM simulations, the mass of particles is often increased by several orders of magnitude, which allows increasing the simulation step [34,40,45,48,53]. Henrich and collaborators [40] have found that the scaling of particle mass S_{m_p} up to $8.6{\cdot}10^{-11}\frac{R^8}{\gamma_s \delta_b}$ can be effectively used. Dosta et al. [34] applied a density scale factor of 10^{13}, which led to a condition $S_{m_p} < 4{\cdot}10^{-11}\frac{R^8}{\gamma_s \Delta_b}$. In the present study, the density was scaled by a factor of $1.8{\cdot}10^{19}$, which satisfies the described requirement. Considering the scaling of mass applied, the TMS model presented stability and convergence for time steps up to $1{\cdot}10^{-3}$ s.

Besides, the number of individual objects is a limiting factor for discrete element approaches [34,40,46,75,76]. Thus, a limitation of about one million particles was imposed in the present work. Hence, the numerical packing was generated by scaling the experimental sample size down. Size correlations dependent on surface area and length were estimated by geometric derivations. Saving the proportions of the experimental and numerical sample dimensions, a quadratic and a linear relationship of the diameters were obtained as the surface area a (Eqn (24)) and length ℓ (Eqn (25)) dependent size correlations:

$$a = \frac{d_{s,exp}^2}{d_{s,num}^2} \quad (24)$$

$$\ell = \frac{d_{s,exp}}{d_{s,num}} \quad (25)$$

To counterbalance the heat exchange given the mass and size scale, the scale parameters S_a and S_ℓ (Eqn (26) and (27)) were calculated by multiplying the size correlations (s. Eqn (24) and (25)) by the particle

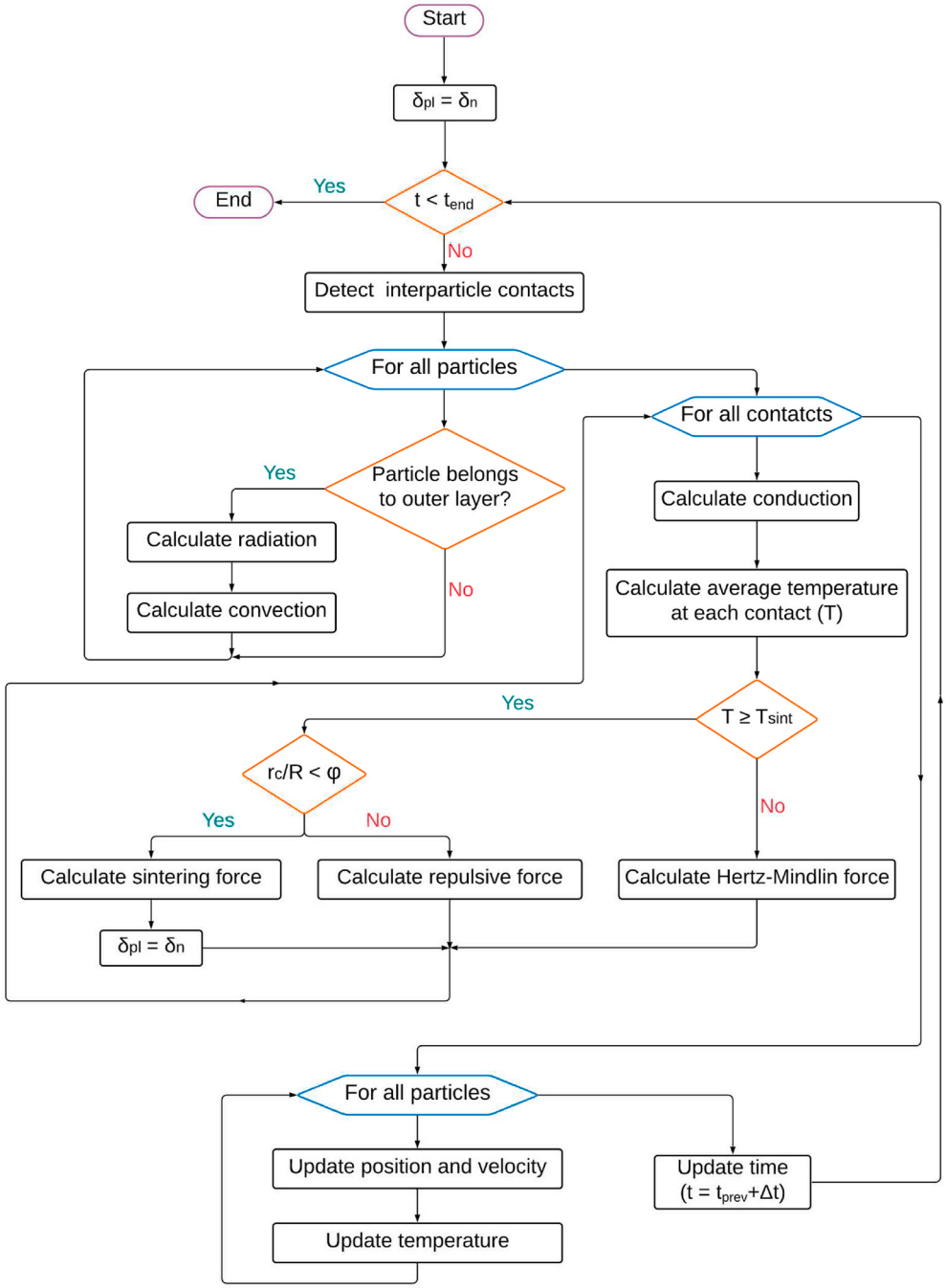

Fig. 2. Schematic representation of the algorithm of the TMS model explicating the main steps.

mass ratio. Substituting $m = \rho V$ for the numerical and experimental geometries, a ratio between the densities multiplied by the size correlation and the volume ratio is obtained. Knowing that the volumes are functions of the respective cubic numerical and experimental diameters, they can be simplified to the diameter with the size correlations. Thus, S_a and S_ℓ assume the final linear and quadratic relationships with the diameters, respectively.

$$S_a = \frac{d_{s,exp}^2\ m_{num}}{d_{s,num}^2\ m_{exp}} = \frac{d_{s,exp}^2\ \rho_{num}\ V_{num}}{d_{s,num}^2\ \rho_{exp} V_{exp}} = \frac{d_{s,num}\rho_{num}}{d_{s,exp}\rho_{exp}} = \frac{d_{s,num}}{d_{s,exp}} S_{m_p} \tag{26}$$

$$S_\ell = \frac{d_{s,exp}\ m_{num}}{d_{s,num}\ m_{exp}} = \frac{d_{s,exp}\ \rho_{num}\ V_{num}}{d_{s,num}\ \rho_{exp} V_{exp}} = \frac{d_{s,num}^2\ \rho_{num}}{d_{s,exp}^2\ \rho_{exp}} = \frac{d_{s,num}^2}{d_{s,exp}^2} S_{m_p} \tag{27}$$

Here $d_{s,exp}$ is the experimental sample diameter, $d_{s,num}$ is the numerical sample diameter, m_{exp} is the mass of Al_2O_3, m_{num} is the mass of numerical particles, ρ_{exp} is the Al_2O_3 density, ρ_{num} is the numerical particle density, V_{num} and V_{exp} are the respective numerical and experimental volumes.

The characteristics of the particles and the packing used here are presented in Table 1. A summary of all the parameters applied to the TMS model and their respective values are given in the Table A.1 in the Appendix.

3. Results and discussion

3.1. Heat transfer and thermal gradients

The fast heating of the numerical specimen before and during rapid sintering is presented in this section. Fig. 3 reveals the profile of temperature evolution in the packing from room temperature to 1050 °C over soaking time. The outer particles hit furnace temperature almost immediately –in less than 10 s– owing to the high heat input by radiation and convection. Heat tended to build up near the outer surface at first. Thus, the temperature in this region increased rapidly while the innermost layers of particles remained essentially at room temperature. Hence, the temperature gradient reached its maximum. Thermal radiation contributes to the heating of particles with the delta of the fourth power of the temperature of transmitting and receiving bodies ($\dot{Q}^{rad} \sim T_{env}^4 - T_{outer}^4$). Therefore, it was indicated as the primary heating source when the cold sample was introduced into the hot furnace. Afterward, the transmission of heat particle by particle via thermal conduction promoted the raising temperature in the inner zone. With the properties and conditions applied, the numerical sample's core reached 48% of furnace temperature in 60 s, and 90% in 240 s. In 540 s – less than 10 min – the entire numerical sample arrived at furnace temperature, and the permanent regime was achieved.

The temperature difference between the sample's surface (T_{outer}) and its center (T_{center}) over time is shown in Fig. 4(a) for both experimental and modeling data. A remarked initial steep thermal gradient was noted due to the low thermal diffusivity of the green Al_2O_3 body [4,16]. Simulation results indicated temperature differences of up to 700 °C after 60 s of soaking time, revealing high thermal gradients within the sample. In 240 s, the thermal difference was still over 145 °C and decreased to less than 10 °C after 540 min. A strong correlation and fitting were observed between the experimental and simulation results, as disclosed by Fig. 4(b). A Pearson's R of 0.994 was obtained, expressing a remarkable degree of linear correlation. Besides, 98.7% of the variation in the simulation result was explained by the regression equation, demonstrating a good fit. The consistent agreement of the numerical and experimental results also reinforced that the thermal model parameters have been appropriately approximated. The statistic coefficients demonstrated the potential of the TMS model in the description of thermal phenomena.

The simulation results of temperature distribution through the Al_2O_3 sample introduced in a pre-heated furnace at 1050 °C, 1250 °C, and 1350 °C are presented in Fig. 5. The temperature difference (y-axis) depicted the furnace temperature subtracted from the average temperature of a set of Al_2O_3 particles placed in equally-sized spherical volumes, which were homogeneously distributed along the radial direction of the numerical sample. Zones near the external surface disclosed lower temperature differences with the furnace, whereas an increased thermal difference was observed moving toward the center. Sample's center, i.e., normalized distance = 0, required a considerable amount of time to achieve furnace temperature (temperature difference = 0). The temperature distribution indicated that heat dynamically transferred along

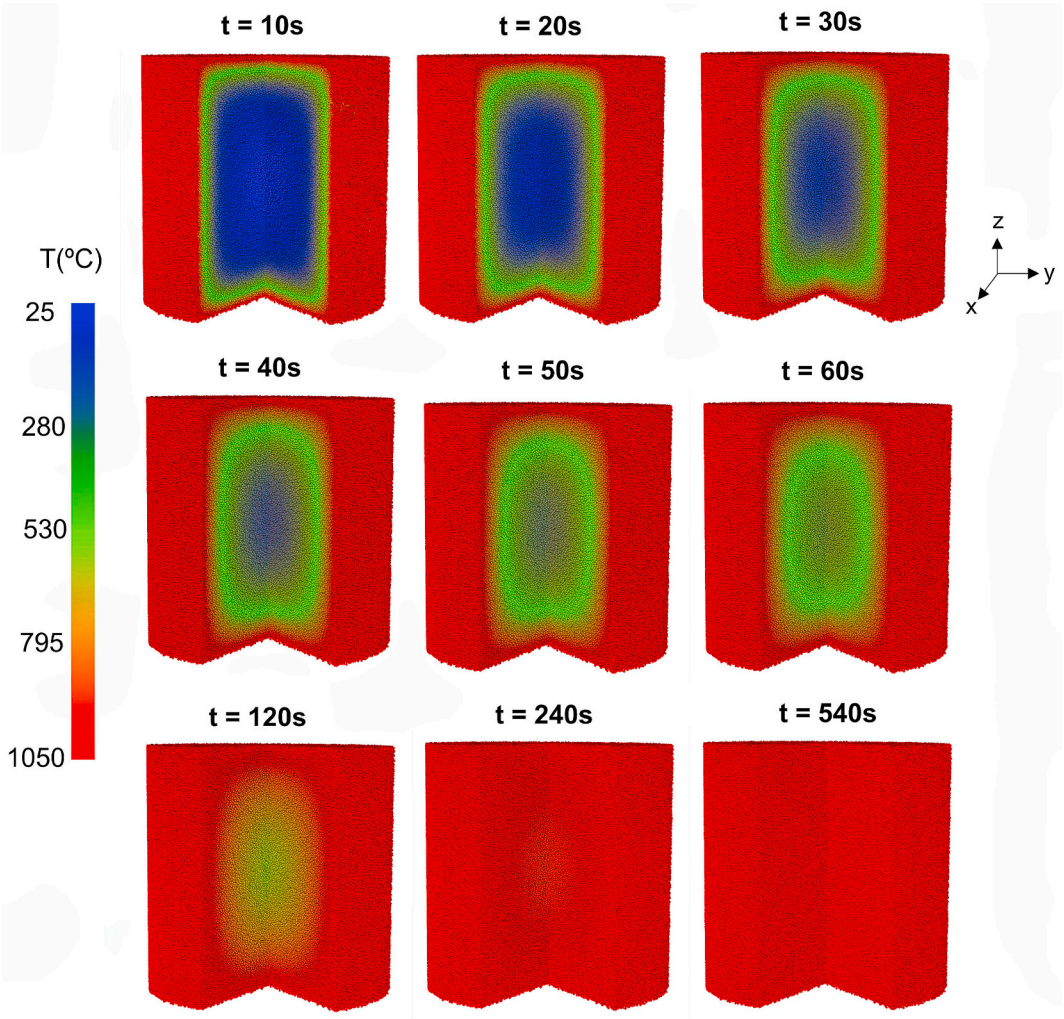

Fig. 3. Profile of temperature evolution over the soaking time at 1050 °C of the numerical alumina sample initially at room temperature.

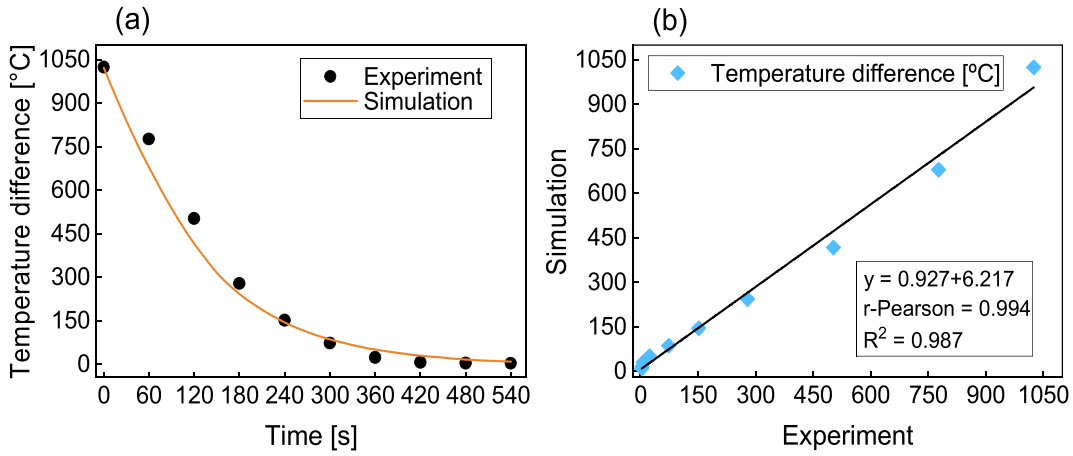

Fig. 4. (a) Difference of temperature between furnace environment and sample's center ($T_{env} - T_{center}$) over soaking time at 1050 °C, and (b) correlation graph – comparison of numerical and experimental [16] results.

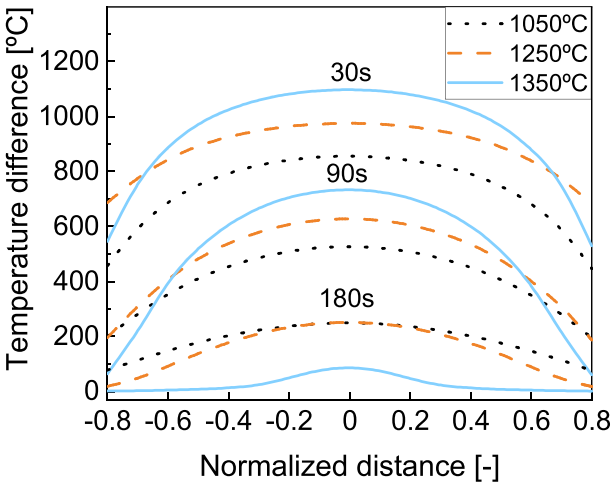

Fig. 5. Progress of temperature profile as a function of sample's position in the radial direction over immersion time at 1050 °C (dotted), 1250 °C (dashed), and 1350 °C (solid). The normalized distance equal to 0 corresponds to the average temperature at the center, whereas negative and positive values represent left- and right-hand sides, respectively.

the sample length from the outer shell towards its core. As a result, the inner particles did not experience the same thermal history as the outer particles most of the time. Hence, the non-isothermal behavior due to temperature gradients along the body was evidenced.

In regions closer to the center (normalized distances between −0.6 and 0.6), the sample sintered at 1350 °C showed higher temperature gradients in the first 90 s, followed by the treatments at 1250 °C and 1050 °C, respectively. Sintering at 1350 °C led to a maximum thermal gradient of ~1100 °C in 30 s at the sample's center. This temperature difference dropped to 750 °C after 90 s. For fast firing at 1250 °C, the temperature gradient reduced from ~1000 °C to 650 °C between 30 and 90s. The lowest thermal gradients in this range were obtained for treatment at 1050 °C. This result showed that the heating flux toward the lower temperature zones is increased as the energy transferred to the compact is amplified, i.e., the higher the sintering/furnace temperature.

Furthermore, increasing the sintering temperature rises the densification of the green ceramic body by enhancing the diffusion process [77–81]. The progress of the densification implies an increase in the local thermal diffusivity leading to a synergistic effect on the heating rate [82]. The boost in thermal diffusivity due to densification causes a substantial enhancement in the speed of heat propagation; therefore, the thermal gradients tend to disappear sooner [4,72]. The decreasing thermal gradient towards the external surface with time at 1350 °C, suggests an increasing thermal diffusivity of Al_2O_3 by the progress of densification from the outwards toward the interior. Treatment at 1050 °C did not lead to densification since this temperature is not high enough to activate sintering mechanisms [16]. Therefore, it took longer for thermal gradients to disappear when compared to treatments at 1250 °C and 1350 °C.

3.2. Microstructure evolution and densification

3.2.1. Micro-macro densification

Numerically accessed microkinetic details can provide additional insights into microstructural development during the intermediate stage of rapid sintering. The evolution of the average coordination number (ACN) and r_c/R along the sample's radial length is disclosed in Fig. 6.

The ACN (Fig. 6 (a)) was constant and equal to 6 along initially. Exposure to the hot environment showed a noticeable increase within 150 s for fast firing at 1350 °C, whereas it took between 150 and 300 s at 1250 °C. The ACN in the most adjacent zone to the outer surface (distance = 0.8) increased from 6 to 8 in just 300 s, reaching 9 closest neighbors after 1200 s at 1350 °C. In contrast, the coordination number remained its initial value closer to the center (distance = 0.2) after 300 s. This demonstrated that the amount of heat propagated to the sample's core in the first 300 s was not enough to cause significant microstructural changes in that region.

The coordination number of the sample sintered at 1250 °C, at a 0.8 normalized distance, increased 1 unit after 300 s and reached approximately 9 at the end. Worth mentioning that a minor variation in ACN along the sample's length was observed when reducing the sintering temperature by 100 °C.

The evolution of r_c/R over the sample's length (Fig. 6 (b)) was notable from 150 s for both sintering temperatures. At this time point, r_c/R essentially kept its initial value in the center, whereas an increase in 2.14 times occurred at a normalized distance of 0.8 at 1350 °C. However, the r_c/R in the center increased by 2.1 times from 150 to 200 s. After 200 s, r_c/R presented a less accentuated gradient between the center and the surface.

For the Al_2O_3 particles sintered at 1250 °C, no variation in r_c/R was observed at the center within the first 200 s. Nevertheless, at the distance of 0.8, there was a 2-fold increase over the same time interval. Significant differences in the center become noticeable only after 300 s.

In summary, the evolution of the coordination number and the r_c/R was not homogeneous throughout the ceramic packing; it rose from the outer surface toward the center during the intermediate stage of sintering. Consequently, it is expected that macroscale densification will

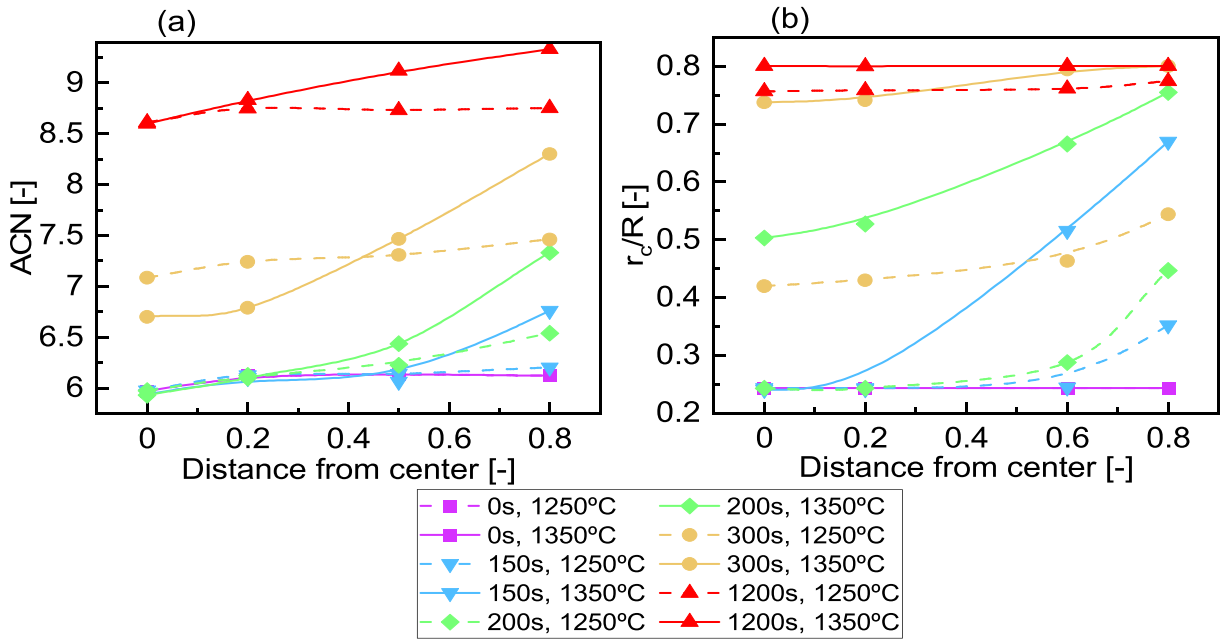

Fig. 6. Evolution of the (a) average coordination number (ACN) and (b) normalized contact radius (r_c/R) over the normalized radial distance from sample's center and dwell time for Al_2O_3 fast-fired at 1250 °C and 1350 °C.

also show this trend, which can be attributed to thermal gradients under the non-isothermal conditions of fast firing. The steep increases of ACN and r_c/R in the zones closer to the outer surface suggest the formation of a densification front that tends to advance in the direction of the thermal gradients, that is, toward the compact interior, controlling further heat flux.

The macroscopic behavior of a ceramic body under fast sintering has its source at the sum of many microscopic interactions between powder particles. The micro-macro dependences were analyzed herein. The numerical results of the relative density over soaking time are shown in Fig. 7(a). The graph considered the heating and sintering stages only. The y-axis outlined the overall increase in bulk density within the whole ceramic body.

The increase in the relative density of the fast sintered sample at

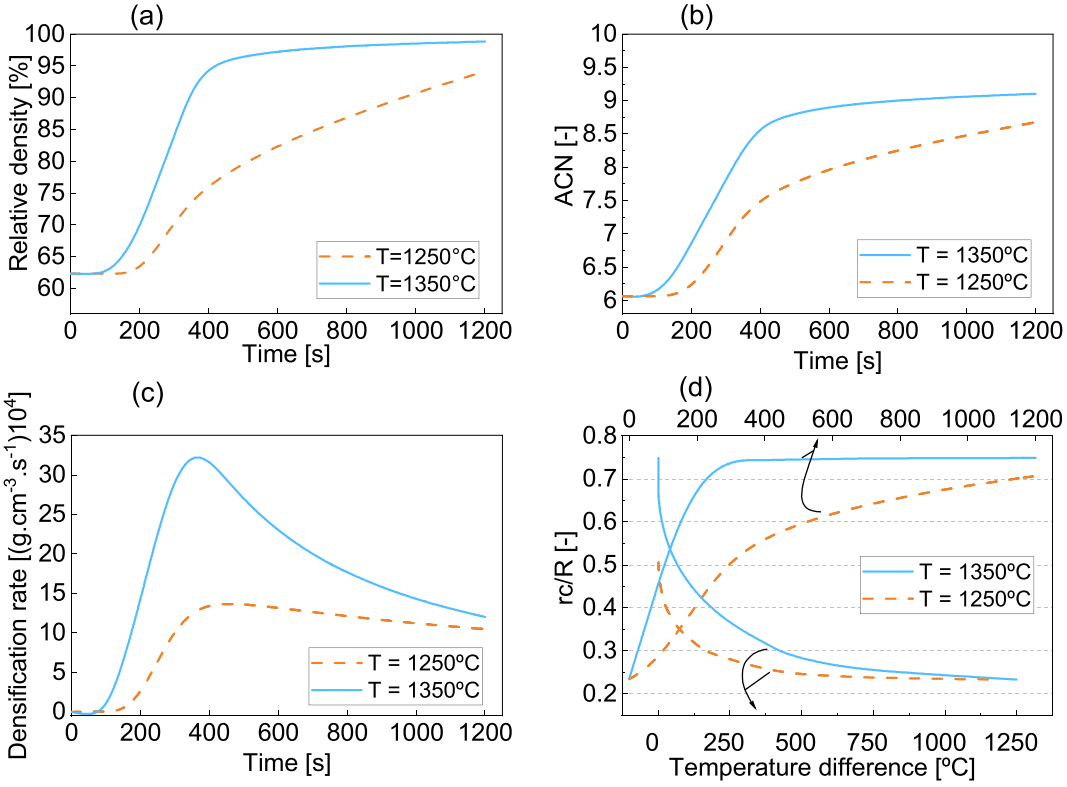

Fig. 7. Numerical evolution of (a) relative density, (b) average coordination number (ACN), (c) densification rate over dwell time, and the (d) progress of the normalized average neck radius (r_c/R) over the temperature difference (bottom x-axis) and sintering time (upper x-axis) at 1250 °C and 1350 °C.

1350 °C began within ~ 100 s of treatment, whereas it took 150 s at 1250 °C. The densification advanced rapidly, achieving 92% of relative density in 350 s for fast firing at 1350 °C. Considering the same time interval, the fast-fired sample at 1250 °C reached 73.5% of relative density. Following, a modest densification trend was observed at 1350 °C until it reaches 98.85% of maximum relative density in 1200 s. Although it progressed at a considerably lower rate than 1350 °C, the treatment at 1250 °C kept a moderate increase in the densification, obtaining 94% of maximum relative density.

The coordination number results from the higher mobility of particles due to the higher sintering driving force [48,49], considering particles of equivalent size, shape, and mass. The steep increase in the relative density was also reflected in the fast increment of the ACN (Fig. 7(b)). The rapid sintering procedure at 1350 °C led to an increase in ACN of 1.4 times in the first 350 s, whereas an increment of 1.2 times was observed at 1250 °C for the same time frame. Nevertheless, the ACN raised by 23% (350–1200 s) at 1250 °C, whereas a modest increase above 13% was observed by increasing sintering temperature in 100 °C. The lessening trend in the dynamic growth rate of the ACN (Fig. 7(b)) and densification (Fig. 7(c)) after 350 s, especially at 1350 °C, suggested that microstructural changes were reaching their maximum. This behavior has been identified experimentally as a 'frozen microstructure point' [20,81] that ceramics might develop when the relative density reaches a certain point. The numerical results showed a frozen point at ~ 92% of relative density, which is consistent with the experimental data of Wang and collaborators [20], in which the 'frozen microstructure point' was found at approximately 95% of relative density for pure sub-micrometric Al_2O_3, fast-fired by the direct-furnace-insertion procedure. On balance, an ACN of 1.5 and 1.4 times was achieved at the end for the fired samples at 1350 °C and 1250 °C, respectively.

Comparatively, a tendency to a sharp increase in the densification rate was registered within the first 350 s at both sintering temperatures, as indicated in Fig. 7(c). The increment of 100 °C at sintering temperature intensified heat input into the particles leading to an increase of almost 61% in the densification rate. Afterward, the densification rate decreased for the sample sintered at 1350 °C while it remained almost constant until the end of the treatment at 1250 °C. At the endpoint (1200 s), the difference between the densification rates of sintering at 1350 and 1250 °C was just 13%.

The progress of the normalized average neck radius r_c/R of the overall particles over the temperature difference and the sintering time is presented in Fig. 7(d). It was observed a 3-fold increase in r_c/R accompanying the temperature gradient regime from 1250 °C to approximated 0 °C in the first 200 s for fast sintering at 1350 °C. The sample sintered at 1250 °C experienced an increase of only 1.75 times in r_c/R for the same time interval, which indicates that the decrease in sintering temperature leads to a delay of 50% in densification within the first 200 s. Besides, it was observed that the sample fired at 1250 °C remained under thermal gradients for 100 s longer. Thus, increasing sintering temperature enhances the densification rate and the speed at which temperature gradients passed throughout the sample.

3.2.2. *Microstructural effects of temperature gradients*

Experimental studies point to a characteristic densification behavior of fast firing [6,7,9] in which a denser shell is formed in the sample surface and moves inwards. The simulation results foresaw this characteristic microstructure owing to forming a densification front in the intermediate stage of fastsintering at 1350 °C, as shown in Fig. 8. A denser outer layer of particles was formed and enveloped the porous inner region (Fig. 8(a)). The highlighted region of the simulation image nicely corresponds to the micrography (Fig. 8(b)) obtained experimentally by García and collaborators [16]. The densification front is the product of thermal gradients generated by the rapid heat input and is pointed as the controller agent of the heat flow within the compact. Thus, forming a dense layer of Al_2O_3 at the interface between the furnace environment and the green sample has a significant effect on the temperature profile distribution. High densification rates observed during fast sintering seem to be related to a change in the sample's internal structure, which is not considered a complementary sintering mechanism but can contribute to the improvement of sintering [16].

3.2.3. *Radial shrinkage*

The radial shrinkage of the simulation samples sintered at 1250 °C and 1350 °C is shown in Fig. 9. The initial stage, 250 s, 350 s, and the last simulation time point are illustrated. The radial shrinkage S_r was defined by Eqn (28) as a function of the cross-section diameter of the cylindrical sample at the beginning $D_{t=0}$ and after each specified time interval $D_{t=x}$.

$$S_r = \frac{D_{t=0} - D_{t=x}}{D_{t=0}} \tag{28}$$

A radial shrinkage of 10% accompanied the increment in the density after 250 s of fast firing at 1350 °C, while this value is 2.2 times smaller when 100 °C decreased the sintering temperature. At 350 s, the radial

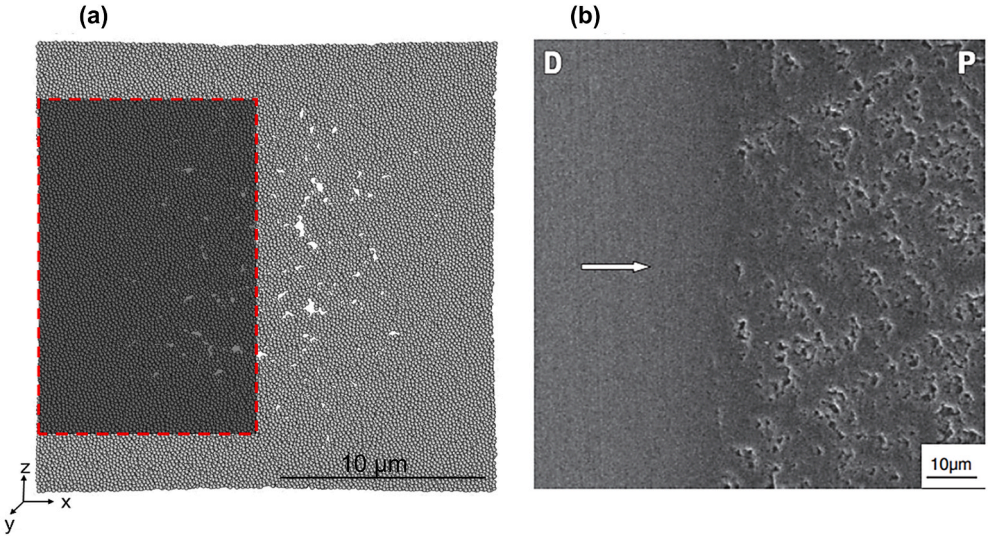

Fig. 8. Visualization of the densification front from (a) the numerical sample by the TMS model, and (b) SEM image of a cross-section of fast-fired Al_2O_3, showing the densification front moving from the dense outer surface D toward the porous center of the sample P [16] (with copyright permission from the journal). The numerical representation is a half-section in the y-axis of the cylindrical sample, with a thickness of 2 layers of particles, at 550 s, and fast-fired at 1350 °C.

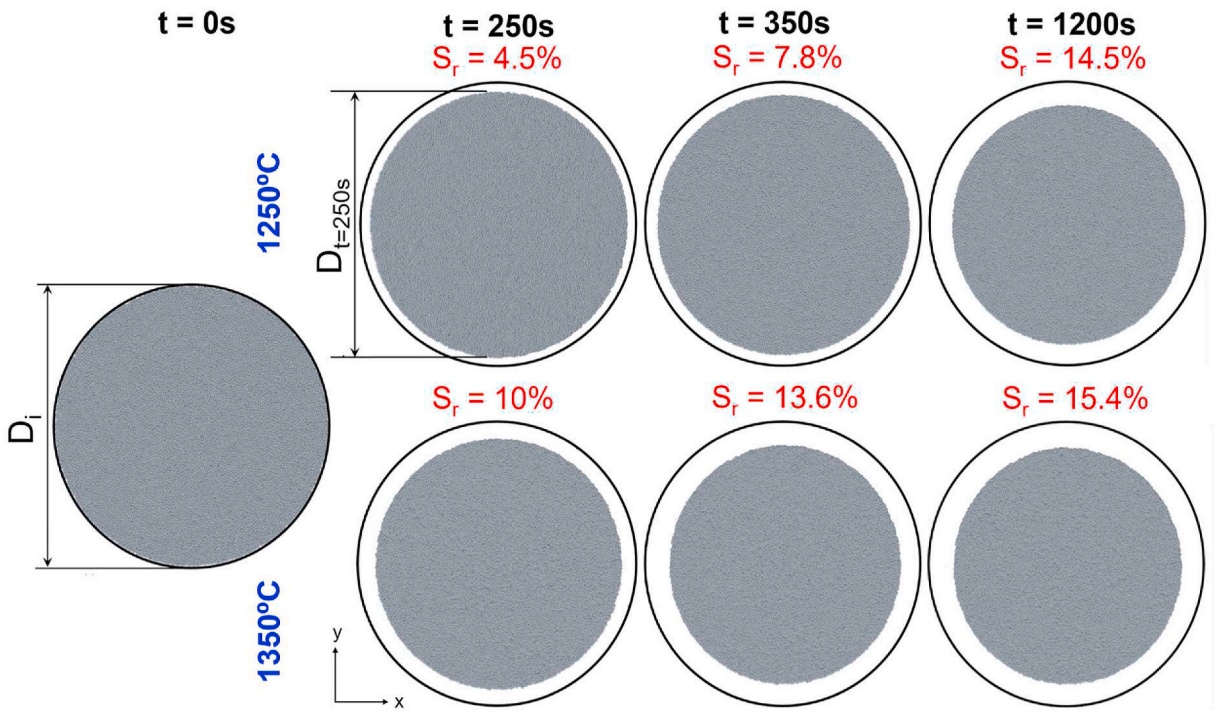

Fig. 9. Visualization of cross-sections of 3D simulation in initial (t = 0s), intermediate (t = 250s, t = 350s) and end-stage (t = 1200s) for the Al_2O_3 samples fast-fired at 1250 °C and 1350 °C. The cross-section view represents the circular section of the cylindrical sample cut in half of its height (z-axis).

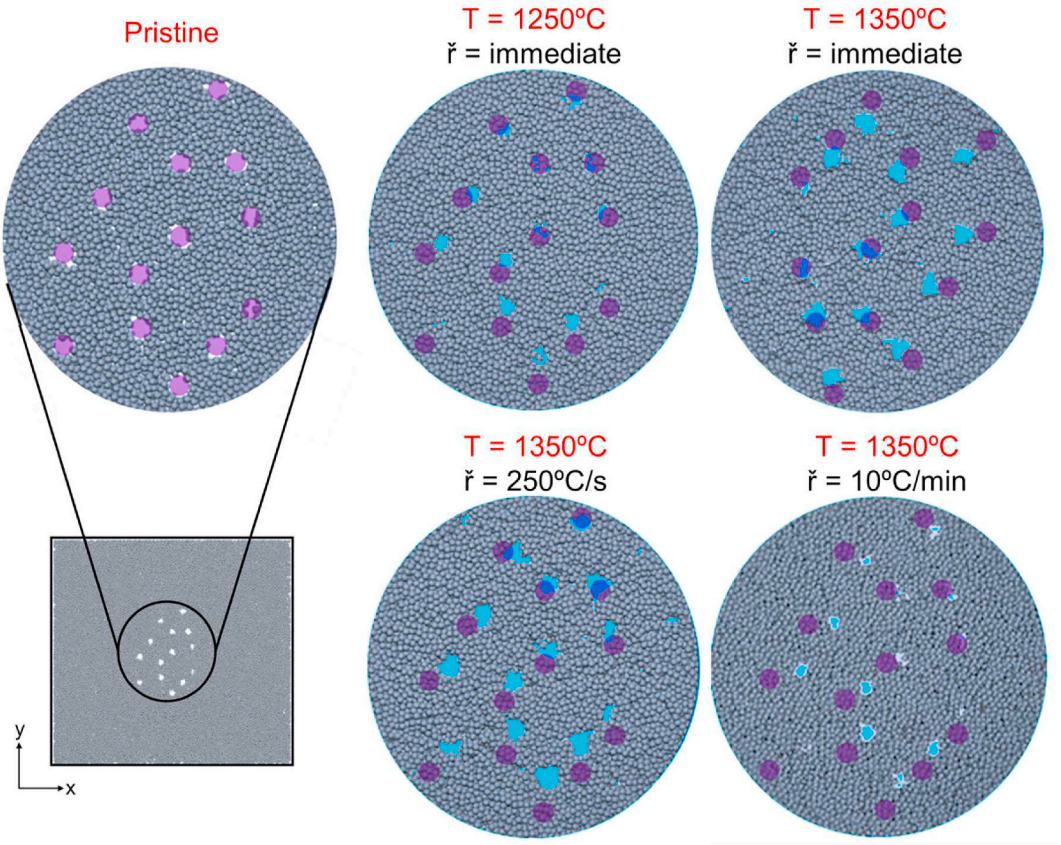

Fig. 10. Microstructural evolution of defects after sintering at different temperatures and heating rates. The pristine sample represents the initial microstructure and the following images refers to the endpoint of each treatment. The defects are purple-colored at the initial condition and cyan after each treatment. The numerical representation is a half-section view in the y-axis of the cylindrical sample with 2 layers of particles thickness. (For interpretation of the references to color in this figure legend, the reader is referred to the Web version of this article.)

shrinkage progressed to 13.6% and 7.8% for fast sintering at 1350 °C and 1250 °C, respectively. After 1200 s, the TMS model forecasted 15.4% of radial shrinkage for the Al_2O_3 body fast-fired at 1350 °C and 14.5% for sintering at 1250 °C. The foretold values for the radial shrinkage agree with the micro-macro densification features discussed beforehand. Furthermore, the shrinkage values predicted by the present method agree with previous experimental work [83,84].

3.2.4. Influence of sintering parameters on microstructural evolution of defects

Randomly distributed mesoscopic defects were artificially introduced by deleting particles inside the initial Al_2O_3 sample with the scope of further analysis of the microstructure development. The defects were created in spherical-shaped regions (purple colored), simulating a sort of internal mesopores. The defects evolution in the final microstructures after sintering at 1350 °C with instantaneous heating rate, 250 °C/s, and 10 °C/min, in contrast with fastsintering at 1250 °C, is depicted in Fig. 10.

Compared to the pristine sample, the morphology of the defects did not present considerable dissimilarity between the high heating rates (instantaneous and 250 °C/s) modeled under fast firing at 1350 °C. However, an essential microstructural evolution with a definite trend to the closure of internal defects was observed by applying a conventional firing protocol ($\check{R}$ = 10 °C/min) at 1350 °C. Decreasing sintering temperature by 100 °C (T_{sint} = 1250 °C) and keeping the instantaneous heating rate, a substantial reduction in the size of the defects was observed, which led to a significant morphological variation in the area of defects with a tendency to obtaining a denser sample.

The antagonistic effect of temperatures and heating rates on the significant evolution of defects under rapid firing may have originated, among other factors, in the fast spread of heat due to high thermal gradients. The abrupt propagation of heat did not provide enough time for activation of specific mechanisms that might have favored mass transfer and the relief of stresses trapped in the region of the defects. Therefore, the higher temperature did not lead to a significant evolution of the defects under rapid firing, which may have originated in the rapid spread of heat due to the high thermal gradients.

4. Conclusion and outlook

An original model for thermomechanics coupled with sintering (TMS) was formulated and implemented in the DEM simulation framework MUSEN. The incorporation of heat transfer concepts, transient temperature regime and sintering allowed the representation of fast sintering kinetics. The TMS model provided new insights into microscale features that contribute to the macro behavior of ceramics under rapid firing.

The simulation results showed relevant details of the densification process concerning sintering temperature, thermal and density gradients, including the evolution of micro-kinetics, named the coordination number and the distribution of the cohesive neck size, and the progress of defects. The TMS model showed a good agreement with experimental data of thermal gradients in the range analyzed. The numerical heating profiles showed that the outer surface reached furnace temperature almost immediately. Afterward, the heat flowed particle by particle toward the sample's core. The densification did not occur homogeneously according to the micro-kinetics investigation over the sample's length; the gradients of density tended to be accentuated at higher sintering temperatures. The densification front phenomenon was also foreseen. The increment in the neck radius and coordination number from the outer layer to the center of the sample confirmed the densification path during the fast firing procedure. The interplay of the microscopic phenomena led to the increase of the overall relative density and shrinkage. Despite the increase in sintering temperature has indicated a positive effect on the relative density, densification rate, and coordination number, higher sintering temperatures did not necessarily represent the best condition for internal defect retrenchment. Indeed, an opposite effect was observed — the substantial enhancement in the speed of heat propagation that caused the thermal gradients to disappear sooner.

The proposed TMS model allows analyzing and predicting microscale phenomena during fast sintering, which are not trivial to be obtained experimentally. This model has high potential to be applied in other systems, including incorporating other mechanisms for rearrangement and densification, such as viscous flow.

Declaration of competing interest

The authors declare that they have no known competing financial interests or personal relationships that could have appeared to influence the work reported in this paper.

Acknowledgments

This work was bi-laterally supported by the Coordination for the Improvement of Higher Education Personnel – CAPES – Brazil and the German Research Foundation – DFG – Germany in the scope of the collaborative research initiative PIPC, project number 88881.207634/2018–01 and project number 418788750 (DFG DO 2026/6–1). We acknowledge Dr. Talita Possamai and Dr. Renato Oba for collaborating with a careful and critical reading and Carine Lourenco for English review.

Appendix

Complementary equations:

$$\delta_n = R_i + R_j - \left|\vec{X}_i - \vec{X}_j\right| \tag{A.1}$$

$$K_n = 2\,E^* \sqrt{R^*\,\delta_n^{HM}} \tag{A.2}$$

$$\beta_n = 1.8257\,\mu\,\sqrt{K_n\,m^*} \tag{A.3}$$

$$K_t = 8\,G^* \sqrt{R^*\,\delta_n^{HM}} \tag{A.4}$$

$$\delta\delta_t = v_{rel,t}\,\Delta t \tag{A.5}$$

$$\beta_t = 1.8257\,\mu\,\sqrt{K_t\,m^*} \tag{A.6}$$

$$\mu = \frac{-\ln^2 e}{\sqrt{\pi^2 + \ln^2 e}} \tag{A.7}$$

$$m^* = \frac{m_i\, m_j}{m_i + m_j} \tag{A.8}$$

$$R^* = \frac{R_i\, R_j}{R_i + R_j} \tag{A.9}$$

$$E^* = \left(\frac{1-\nu_i^2}{E_i} + \frac{1-\nu_j^2}{E_j}\right)^{-1} \tag{A.10}$$

$$G^* = \left(\frac{2-\nu_i}{G_i} + \frac{2-\nu_j}{G_j}\right)^{-1} \tag{A.11}$$

Here, E^*, R^*, m^*, and G^* are the equivalent Young's modulus, radius, mass, and shear modulus of the two contacting bodies, e is the restitution coefficient, and ν is Poisson's ratio.

Table A.1
Summary of TMS model parameters.

Parameters	Symbol	Unit	Value
Convective heat transfer	h_c	$W/m^2{\cdot}K$	5
Surface emissivity	ε	–	0.8
Stefan-Boltzmann constant	σ	$W/m^2{\cdot}K^4$	$5.67{\cdot}10^{-8}$
Initial temperature of particles	T_o	K	298
Inner temperature of furnace	T_{env}	K	1323.15–1623.15
Heating rate	$\dot{R}$	°C/s	0.17-Instant.
Thermal conduction resistivity factor	f_{res}	–	0.18
Minimum average normal overlap	λ_{min}	–	0.03
Maximum average normal overlap	λ_{max}	–	0.05
Factor of size scaling for surface dependency	S_a	–	$1.1{\cdot}10^{-3}$
Factor of size scaling for length dependency	S_ℓ	–	$1.21{\cdot}10^{-6}$
Slip parameter	η	–	0.01
Sintering model parameter	α	–	4
Sintering model parameter	β	–	4.5
Minimum temperature for sintering	T_{min}^{sint}	K	1373.15
Stop criterion	$\max\ r_c/R$	–	0.8
Initial temperature	T_0	K	298.15–373.15
Treatment temperature	T	K	1523.15–1623.15
Factor of mass scaling	S_{m_p}	–	$1.8{\cdot}10^{19}$
Restitution coefficient	e	–	0.1
Poisson's ratio	ν	–	0.23
Simulation time step	Δt	s	0.001

Author contributions

Conceptualization: M.H.P.T., M.D., D.H., R.J., S.Y.G.G., A.D.N.J., and J.B.R.N.; Methodology: M.H.P.T., V.S., and M.D.; Software: V.S. and M.D.; Formal analysis: M.H.P.T., V.S., and M.D.; Investigation: M.H.P.T., V.S., and M.D.; Resources: R.J., S.Y.G.G., A.D.N.J, J.B.R.N., D.H., and M.D.; Data Curation: M.H.P.T., V.S., and M.D.; Draft preparation and writing: M.H.P.T.; Review and editing: R.J., S.Y.G.G., A.D.N.J, J.B.R.N., D.H., V.S., and M.D.; Supervision: D.H., and M.D.; Project coordination: M.D., and A.D.N.J; Funding acquisition: R.J., S.Y.G.G., A.D.N.J, J.B.R.N., D.H., and M.D.

References

[1] R.M. German, J.F. Lathrop, Simulation of spherical powder sintering by surface diffusion, J. Mater. Sci. 13 (1978) 921–929, https://doi.org/10.1007/BF00544686.

[2] R.M. German, Thermodynamics of sintering, in: Z.Z. Fang (Ed.), Sinter. Adv. Mater. Fundam. Process., first ed., Woodhead Publishing Limited, 2010, pp. 3–473, https://doi.org/10.1533/9781845699949.1.3.

[3] R. Grupp, M. Nöthe, B. Kieback, J. Banhart, Cooperative material transport during the early stage of sintering, Nat. Commun. 2 (2011), https://doi.org/10.1038/ncomms1300.

[4] T.S. Possamai, R. Oba, V.P. Nicolau, D. Hotza, D.E. García, Numerical simulation of the fast firing of alumina in a box furnace, J. Am. Ceram. Soc. 95 (2012) 3750–3757, https://doi.org/10.1111/j.1551-2916.2012.05432.x.

[5] S.Y. Gómez, A.L. Da Silva, D. Gouvêa, R.H.R. Castro, D. Hotza, Nanocrystalline yttria-doped zirconia sintered by fast firing, Mater. Lett. 166 (2016) 196–200, https://doi.org/10.1016/j.matlet.2015.12.042.

[6] L. Camm, Adventures in fast firing, Ceram. Refract. (2017). https://www.industrialheating.com/articles/95372-adventures-in-fast-firing.

[7] G.J. Ghorra, Theory of fast firing, Ceram. Eng. Sci. Proc. 115 (2008) 77–115, https://doi.org/10.1002/9780470314050.ch9.

[8] K.K. Singh, Subrahmanyam, Fast firing of ceramics—a review, Trans. Indian Ceram. Soc. 35 (1976) 26–30, https://doi.org/10.1080/0371750X.1976.10840848.

[9] D.E. García, J. Seidel, R. Janssen, N. Claussen, Fast firing of alumina, J. Eur. Ceram. Soc. 15 (1995) 935–938, https://doi.org/10.1016/0955-2219(95)00071-2.

[10] M.F. Pinto, S.J.G. Sousa, J.N.F. Holanda, Efeito do ciclo de queima sobre as propriedades tecnológicas de uma massa cerâmica vermelha para revestimento poroso, Cerâmica 51 (2005) 225–229, https://doi.org/10.1590/s0366-69132005000300009.

[11] A. Seal, R. Mazumder, A. Sen, H.S. Maiti, Fast firing of lead zirconate titanate ceramics at low temperature, Mater. Chem. Phys. 97 (2006) 14–18, https://doi.org/10.1016/j.matchemphys.2005.05.038.

[12] R.P.S. Dutra, M.L. Varela, R.M. Nascimento, U.U. Gomes, A.E. Martinelli, C. A. Paskocimas, Estudo comparativo da queima rápida com a queima tradicional nas propriedades de materiais cerâmicos de base argilosa, Cerâmica 55 (2009) 100–105, https://doi.org/10.1590/s0366-69132009000100014.

[13] J. Zhang, F. Meng, R.I. Todd, Z. Fu, The nature of grain boundaries in alumina fabricated by fast sintering, Scripta Mater. 62 (2010) 658–661, https://doi.org/10.1016/j.scriptamat.2010.01.019.

[14] M. Dondi, M. Marsigli, I. Venturi, Microstructure and mechanical properties of clay bricks: comparison between fast firing and traditional firing, Br. Ceram. Trans. 98 (1999) 12–18, https://doi.org/10.1179/bct.1999.98.1.12.

[15] E. Bernardo, G. Scarinci, Fast sinter crystallisation of waste glasses, Adv. Appl. Ceram. 107 (2008) 344–349, https://doi.org/10.1179/174367508X289451.

[16] D.E. García, D. Hotza, R. Janssen, Building a sintering front through fast firing, Int. J. Appl. Ceram. Technol. 8 (2011) 1486–1493, https://doi.org/10.1111/j.1744-7402.2011.02609.x.

[17] R. Anderson, L. Bates, E. Johnson, J.F. Morris, Packed bed thermal energy storage: a simplified experimentally validated model, J. Energy Storage. 4 (2015) 14–23, https://doi.org/10.1016/j.est.2015.08.007.

[18] L. Chen, C. Wang, M. Moscardini, M. Kamlah, S. Liu, A DEM-based heat transfer model for the evaluation of effective thermal conductivity of packed beds filled with stagnant fluid: thermal contact theory and numerical simulation, Int. J. Heat Mass Tran. 132 (2019) 331–346, https://doi.org/10.1016/j.ijheatmasstransfer.2018.12.005.

[19] Y.T. Feng, K. Han, D.R.J. Owen, Discrete thermal element modelling of heat conduction in particle systems: pipe-network model and transient analysis, Powder Technol. 193 (2009) 248–256, https://doi.org/10.1016/j.powtec.2009.03.001.

[20] L. Wang, J. Sun, Numerical simulation of radiation heat transfer characteristics in a cylindrical fluidized bed, Heat Mass Transf. Und Stoffuebertragung. 56 (2020) 2025–2034, https://doi.org/10.1007/s00231-020-02822-z.

[21] M. Moscardini, Y. Gan, S. Pupeschi, M. Kamlah, Discrete element method for e ff ective thermal conductivity of packed pebbles accounting for the Smoluchowski e ff ect, Fusion Eng. Des. 127 (2018) 192–201, https://doi.org/10.1016/j.fusengdes.2018.01.013.

[22] P.G. Rousseau, C.G. Du Toit, W. Van Antwerpen, H.J. Van Antwerpen, Separate effects tests to determine the effective thermal conductivity in the PBMR HTTU test facility, Nucl. Eng. Des. 271 (2014) 444–458, https://doi.org/10.1016/j.nucengdes.2013.12.015.

[23] C. Sangrós, C. Schilde, A. Kwade, Effect of microstructure on thermal conduction within lithium-ion battery electrodes using discrete element method simulations, Energy Technol. 4 (2016) 1611–1619, https://doi.org/10.1002/ente.201600144.

[24] I. Terreros, I. Iordanoff, J.L. Charles, Simulation of continuum heat conduction using DEM domains, Comput. Mater. Sci. 69 (2013) 46–52, https://doi.org/10.1016/j.commatsci.2012.11.021.

[25] Y. Tsuji, T. Tanaka, T. Ishida, Lagrangian numerical simulation of plug flow of cohesionless particles in a horizontal pipe, Powder Technol. 71 (1992) 239–250, https://doi.org/10.1016/0032-5910(92)88030-L.

[26] W.L. Vargas, J.J. McCarthy, Conductivity of granular media with stagnant interstitial fluids via thermal particle dynamics simulation, Int. J. Heat Mass Tran. 45 (2002) 4847–4856, https://doi.org/10.1016/S0017-9310(02)00175-8.

[27] H. Wu, N. Gui, X. Yang, J. Tu, S. Jiang, Numerical simulation of heat transfer in packed pebble beds: CFD-DEM coupled with particle thermal radiation, Int. J. Heat Mass Tran. 110 (2017) 393–405, https://doi.org/10.1016/j.ijheatmasstransfer.2017.03.035.

[28] Q. Zhou, H.W. Zhang, Y.G. Zheng, A homogenization technique for heat transfer in periodic granular materials, Adv. Powder Technol. 23 (2012) 104–114, https://doi.org/10.1016/j.apt.2011.01.002.

[29] H. Haddad, W. Leclerc, G.A. Hassan, A. Ammar, C. Pélegris, M. Guessasma, E. Bellenger, Numerical investigation of heat conduction in heterogeneous media with a discrete element method approach, Int. J. Therm. Sci. 164 (2021), https://doi.org/10.1016/j.ijthermalsci.2020.106799.

[30] H. Haddad, M. Guessasma, J. Fortin, Heat transfer by conduction using DEM-FEM coupling method, Comput. Mater. Sci. 81 (2014) 339–347, https://doi.org/10.1016/j.commatsci.2013.08.033.

[31] M. Kiani-Oshtorjani, P. Jalali, Thermal discrete element method for transient heat conduction in granular packing under compressive forces, Int. J. Heat Mass Tran. 145 (2019) 118753, https://doi.org/10.1016/j.ijheatmasstransfer.2019.118753.

[32] R. Besler, M.R. da Silva, M. Dosta, S. Heinrich, R. Janssen, Discrete element simulation of metal ceramic composite materials with varying metal content, J. Eur. Ceram. Soc. 36 (2016) 2245–2253, https://doi.org/10.1016/j.jeurceramsoc.2015.12.051.

[33] R. Besler, M. Rossetti Da Silva, J.J. Do Rosario, M. Dosta, S. Heinrich, R. Janssen, Sintering simulation of periodic macro porous alumina, J. Am. Ceram. Soc. 98 (2015) 3496–3502, https://doi.org/10.1111/jace.13684.

[34] M. Dosta, K.P. Furlan, V. Skorych, S. Heinrich, R. Janssen, Influence of pores arrangement on stability of photonic structures during sintering, J. Eur. Ceram. Soc. 40 (2020) 4562–4571, https://doi.org/10.1016/j.jeurceramsoc.2020.04.019.

[35] D. Jauffrès, C.L. Martin, A. Lichtner, R.K. Bordia, Simulation of the toughness of partially sintered ceramics with realistic microstructures, Acta Mater. 60 (2012) 4685–4694, https://doi.org/10.1016/j.actamat.2012.05.024.

[36] K. Mori, Finite element simulation of powder forming and sintering, Comput. Methods Appl. Mech. Eng. 195 (2006) 6737–6749, https://doi.org/10.1016/j.cma.2005.10.015.

[37] T. Rasp, T. Kraft, H. Riedel, Discrete element study on the influence of initial coordination numbers on sintering behaviour, Scripta Mater. 69 (2013) 805–808, https://doi.org/10.1016/j.scriptamat.2013.09.003.

[38] T. Rasp, C. Jamin, O. Guillon, T. Kraft, Cracking and shape deformation of cylindrical cavities during constrained sintering, J. Eur. Ceram. Soc. 37 (2017) 2907–2917, https://doi.org/10.1016/j.jeurceramsoc.2017.03.013.

[39] R. Ganeriwala, T.I. Zohdi, A coupled discrete element-finite difference model of selective laser sintering, Granul. Matter 18 (2016) 1–15, https://doi.org/10.1007/s10035-016-0626-0.

[40] B. Henrich, A. Wonisch, T. Kraft, M. Moseler, H. Riedel, Simulations of the influence of rearrangement during sintering, Acta Mater. 55 (2007) 753–762, https://doi.org/10.1016/j.actamat.2006.09.005.

[41] M. Weber, A. Spettl, M. Dosta, S. Heinrich, V. Schmidt, Simulation-based investigation of core-shell agglomerates: influence of spatial heterogeneity in particle sizes on breakage characteristics, Comput. Mater. Sci. 137 (2017) 100–106, https://doi.org/10.1016/j.commatsci.2017.05.014.

[42] F. Parhami, R.M. McMeeking, A network model for initial stage sintering, Mech. Mater. 27 (1998) 111–124, https://doi.org/10.1016/S0167-6636(97)00034-3.

[43] C.L. Martin, L.C.R. Schneider, L. Olmos, D. Bouvard, Discrete element modeling of metallic powder sintering, Scripta Mater. 55 (2006) 425–428, https://doi.org/10.1016/j.scriptamat.2006.05.017.

[44] S. Martin, S. Navarro, H. Palancher, A. Bonnin, J. Léchelle, M. Guessasma, J. Fortin, K. Saleh, Validation of DEM modeling of sintering using an in situ X-ray microtomography analysis of the sintering of NaCl powder, Comput. Part. Mech. 3 (2016) 525–532, https://doi.org/10.1007/s40571-015-0062-7.

[45] S. Martin, M. Guessasma, J. Léchelle, J. Fortin, K. Saleh, F. Adenot, Simulation of sintering using a non smooth discrete element method. Application to the study of rearrangement, Comput. Mater. Sci. 84 (2014) 31–39, https://doi.org/10.1016/j.commatsci.2013.11.050.

[46] A. Wonisch, O. Guillon, T. Kraft, M. Moseler, H. Riedel, J. Rödel, Stress-induced anisotropy of sintering alumina: discrete element modelling and experiments, Acta Mater. 55 (2007) 5187–5199, https://doi.org/10.1016/j.actamat.2007.05.038.

[47] A. Lichtner, D. Roussel, D. Röhrens, D. Jauffres, J. Villanova, C.L. Martin, R. K. Bordia, Anisotropic sintering behavior of freeze-cast ceramics by optical dilatometry and discrete-element simulations, Acta Mater. 155 (2018) 343–349, https://doi.org/10.1016/j.actamat.2018.06.001.

[48] C.L. Martin, R.K. Bordia, The effect of a substrate on the sintering of constrained films, Acta Mater. 57 (2009) 549–558, https://doi.org/10.1016/j.actamat.2008.09.041.

[49] F. Parhami, R.M. McMeeking, A.C.F. Cocks, Z. Suo, A model for the sintering and coarsening of rows of spherical particles, Mech. Mater. 31 (1999) 43–61, https://doi.org/10.1016/S0167-6636(98)00049-0.

[50] S. Nosewicz, J. Rojek, K. Pietrzak, M. Chmielewski, Viscoelastic discrete element model of powder sintering, Powder Technol. 246 (2013) 157–168, https://doi.org/10.1016/j.powtec.2013.05.020.

[51] S. Nosewicz, J. Rojek, M. Chmielewski, Discrete element framework for determination of sintering and postsintering residual stresses of particle reinforced composites, Materials 13 (2020) 1–21, https://doi.org/10.3390/ma13184015.

[52] J. Rojek, S. Nosewicz, M. Maździarz, P. Kowalczyk, K. Wawrzyk, D. Lumelskyj, Modeling of a sintering process at various scales, Procedia Eng. 177 (2017) 263–270, https://doi.org/10.1016/j.proeng.2017.02.210.

[53] V. Iacobellis, A. Radhi, K. Behdinan, Discrete element model for ZrB2-SiC ceramic composite sintering, Compos. Struct. 229 (2019) 111373, https://doi.org/10.1016/j.compstruct.2019.111373.

[54] M. Dosta, V. Skorych, MUSEN: an open-source framework for GPU-accelerated DEM simulations, Software 12 (2020) 100618, https://doi.org/10.1016/j.softx.2020.100618.

[55] S. Kozhar, M. Dosta, S. Antonyuk, S. Heinrich, U. Bröckel, DEM simulations of amorphous irregular shaped micrometer-sized titania agglomerates at compression, Adv. Powder Technol. 26 (2015) 767–777, https://doi.org/10.1016/j.apt.2015.05.005.

[56] S. Dranishnykov, M. Dosta, Advanced approach for simulation results saving from discrete element method, Adv. Eng. Software 136 (2019) 102694, https://doi.org/10.1016/j.advengsoft.2019.102694.

[57] R.G. Munro, Evaluated material properties for a sintered alpha-alumina, J. Am. Ceram. Soc. 80 (1997) 1919–1928, https://doi.org/10.1111/j.1151-2916.1997.tb03074.x.

[58] Z. Peng, E. Doroodchi, B. Moghtaderi, Heat transfer modelling in Discrete Element Method (DEM)-based simulations of thermal processes: theory and model development, Prog. Energy Combust. Sci. 79 (2020), https://doi.org/10.1016/j.pecs.2020.100847.

[59] T.L. Bergman, A.S. Lavine, Fundamentals of Heat and Mass Transfer, eighth ed., John Wiley & Sons, Inc., United States of America, 2017.

[60] G.K. Batchelor, R.W. O'Brien, Thermal or electrical conduction through a granular material, Proc. R Soc. Lond. Ser. A 355 (1977) 313–333, https://doi.org/10.1098/rspa.1977.0100.

[61] Y. Liang, X. Li, A new model for heat transfer through the contact network of randomly packed granular material, Appl. Therm. Eng. (2014), https://doi.org/10.1016/j.applthermaleng.2014.08.063.

[62] C.L. Martin, Z. Yan, D. Jauffres, D. Bouvard, R.K. Bordia, Sintered ceramics with controlled microstructures: numerical investigations with the discrete element method, J. Ceram. Soc. Japan. 124 (2016) 340–345, https://doi.org/10.2109/jcersj2.15269.

[63] R.L. Coble, Initial sintering of alumina and hematite, J. Am. Ceram. Soc. 41 (1958) 55–62.

[64] M. Bahrami, J.R. Culham, M.M. Yovanovich, Modeling thermal contact resistance: a scale analysis approach, J. Heat Tran. 126 (2004) 896–905, https://doi.org/10.1115/1.1795238.

[65] R. Askari, S.H. Hejazi, M. Sahimi, Effect of deformation on the thermal conductivity of granular porous media with rough grain surface, Geophys. Res. Lett. 44 (2017) 8285–8293, https://doi.org/10.1002/2017GL074651.

[66] A. Di Renzo, F. Paolo Di Maio, An improved integral non-linear model for the contact of particles in distinct element simulations, Chem. Eng. Sci. 60 (2005) 1303–1312, https://doi.org/10.1016/j.ces.2004.10.004.
[67] R.D. Mindlin, H. Deresiewicz, Elastic spheres in contact under varying oblique force, J. Appl. Mech. Trans. ASM (1953) 327–344.
[68] C.L. Martin, H. Camacho-Montes, L. Olmos, D. Bouvard, R.K. Bordia, Evolution of defects during sintering: discrete element simulations, J. Am. Ceram. Soc. 92 (2009) 1435–1441, https://doi.org/10.1111/j.1551-2916.2009.03014.x.
[69] D. Bouvard, R.M. McMeeking, Deformation of interparticle necks by diffusion-controlled creep, J. Am. Ceram. Soc. 79 (1996) 666–672, https://doi.org/10.1111/j.1151-2916.1996.tb07927.x.
[70] F. Raether, P. Schulze Horn, Investigation of sintering mechanisms of alumina using kinetic field and master sintering diagrams, J. Eur. Ceram. Soc. 29 (2009) 2225–2234, https://doi.org/10.1016/j.jeurceramsoc.2009.01.025.
[71] D. Wang, X. Wang, C. Xu, Z. Fu, J. Zhang, Densification mechanism of the ultra-fast sintering dense alumina, AIP Adv. 10 (2020), https://doi.org/10.1063/1.5119030.
[72] D.E. García, A.N. Klein, D. Hotza, Advanced ceramics with dense and fine-grained microstructures through fast firing, Rev. Adv. Mater. Sci. 30 (2012) 273–281.
[73] M. Dosta, M. Weber, V. Schmidt, S. Antonyuk, DEM Analysis of Breakage Behavior of Bicomponent Agglomerates, Springer International Publishing, 2019, https://doi.org/10.1007/978-3-030-15899-6.
[74] C. O'Sullivan, J.D. Bray, Selecting a suitable time step for discrete element simulations that use the central difference time integration scheme, Eng. Comput. 21 (2004) 278–303, https://doi.org/10.1108/02644400410519794.
[75] B.C. Burman, P.A. Cundall, O.D.L. Strack, A discrete numerical model for granular assemblies, Geotechnique 30 (1980) 331–336, https://doi.org/10.1680/geot.1980.30.3.331.
[76] M. Dosta, R. Besler, C. Ziehdorn, R. Janßen, S. Heinrich, Approximation of mechanical properties of sintered materials with discrete element method, EPJ Web Conf. 140 (2017), https://doi.org/10.1051/epjconf/201714015022.
[77] S.I. Bae, S. Baik, Sintering and grain growth of ultrapure alumina, J. Mater. Sci. 28 (1993) 4197–4204, https://doi.org/10.1007/BF00351254.
[78] O. Gillia, D. Bouvard, Phenomenological analysis of densification kinetics during sintering: application to WC-Co mixture, Mater. Sci. Eng. 279 (2000) 185–191, https://doi.org/10.1016/S0921-5093(99)00621-8.
[79] W. Ji, B. Parker, S. Falco, J.Y. Zhang, Z.Y. Fu, R.I. Todd, Ultra-fast firing: effect of heating rate on sintering of 3YSZ, with and without an electric field, J. Eur. Ceram. Soc. 37 (2017) 2547–2551, https://doi.org/10.1016/j.jeurceramsoc.2017.01.033.
[80] Z. Qing, W. Zhou, W. Xia, H. Li, Crystallization kinetics, sintering, microstructure, and properties of low temperature co-fired magnesium aluminum silicate glass-ceramic, J. Non-Cryst. Solids 486 (2018) 14–18, https://doi.org/10.1016/j.jnoncrysol.2018.02.006.
[81] X.-H. Wang, I.-W. Chen, Sintering dense nanocrystalline ceramics without final-stage grain growth, Nature 404 (2000) 168–171.
[82] G. Moskal, M. Mikuśkiewicz, A. Jasik, Thermal diffusivity measurement of ceramic materials used in spraying of TBC systems: the influence of materials' morphology and (re)manufacturing processes, J. Therm. Anal. Calorim. 138 (2019) 4261–4269, https://doi.org/10.1007/s10973-019-08589-8.
[83] J. Tatami, Y. Suzuki, T. Wakihara, T. Meguro, K. Komeya, Control of shrinkage during sintering of alumina ceramics based on Master Sintering Curve theory, Key Eng. Mater. (2006) 11–14, 317–318, https://doi.org/10.4028/www.scientific.net/kem.317-318.11.
[84] K. Somton, K. Dateraksa, P. Laoratanakul, R. McCuiston, Shrinkage and properties of die pressed alumina produced from different granule sources, AIP Conf. Proc. 2279 (2020), https://doi.org/10.1063/5.0023313.